Electronic Supplementary Material (ESI) for Soft Matter.
This journal is © The Royal Society of Chemistry 2024

Supplementary information for "Heterogeneous Solvent Dissipation Coupled with Particle Rearrangement in Shear Thinning Non-Brownian Suspensions"

A Simulations with a finer spatial resolution

All the results presented in the main text were obtained through hydrodynamic simulations with the numerical mesh size ℓ set to 1. To briefly assess the impact of the mesh size on these simulation results, additional simulations were performed with half the mesh size ($\ell = 0.5$). For $\ell = 0.5$, we set the total number of the grid points to be the same as that employed in the main text (512×512), whereby the system's linear dimension is $L = 256$. Given the existence of system size dependence, which is more significant for larger ϕ, we also conducted simulations with $\ell = 1$ and $L = 256$ to directly compare the results between systems under consistent linear dimensions L but different mesh sizes ℓ. Figure S1(a) displays the viscosity measured at the walls as a function of the shear rate, showing negligible differences in $\eta(\dot{\gamma})$ between $\ell = 1$ and 0.5. As mentioned above, $\eta(\dot{\gamma})$ depends on system size and is slightly larger for $L = 256$ than for $L = 512$ (please see Fig. 1(b) in the main text). Figure S1(b) shows a typical snapshot of a spatial pattern of $i_2/\dot{\gamma}^2$, which is similar to those obtained for $\ell = 1$ shown in Fig. 2 in the main text.

The present results suggest little impact from variations in ℓ; however, this is not conclusive due to the limited range of ℓ values examined. As ℓ decreases, the necessary time step required to maintain numerical stability for solving Navier-Stokes equation decreases significantly, making further assessments increasingly difficult. Examining the mesh size dependence for smaller ℓ remains as a future task.

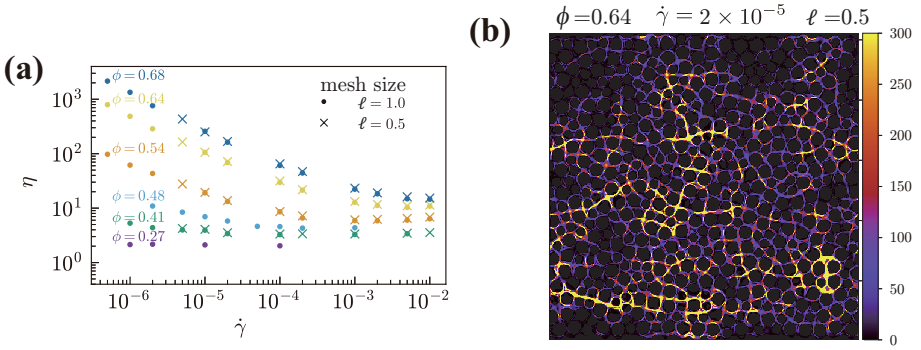

Fig. S1 (a) The viscosity measured at the walls $\eta(\phi)$ for varous ϕ for two different mesh size: the closed circles and crosses represent the results for the mesh sizes $\ell = 1$ and 0.5, respectively. They are almost correspond to each other. (b) A typical snapshot of $i_2/\dot{\gamma}^2$ at $\phi = 0.64$ and $\dot{\gamma} = 2 \times 10^{-5}$ for $\ell = 0.5$.

B Microstructures under shear flow

In this section, we examine how the microstructures are modulated by varying the shear rate $\dot{\gamma}$ through investigations of the partial pair distribution function (PDF) defined for both the same and different species as[1]

$$g_{\mu\mu}(\boldsymbol{r}) = \frac{\hat{\mathcal{A}}}{\hat{N}_\mu(\hat{N}_\mu - 1)} \sum_{i\in\mu}{}' \sum_{j(\neq i)\in\mu}{}' \langle \delta(\boldsymbol{r} - \boldsymbol{r}_i^{(\mu)} + \boldsymbol{r}_j^{(\mu)}) \rangle, \tag{S1}$$

and

$$g_{\mathrm{SL}}(\boldsymbol{r}) = \langle \frac{\hat{\mathcal{A}}}{\hat{N}_\mathrm{S}\hat{N}_\mathrm{L}} \sum_{i\in\mathrm{S}}{}' \sum_{j\in\mathrm{L}}{}' \delta(\boldsymbol{r} - \boldsymbol{r}_i^{(\mathrm{S})} + \boldsymbol{r}_j^{(\mathrm{L})}) \rangle, \tag{S2}$$

respectively. Here, $\boldsymbol{r}_i^{(\mu)}$ represents the position of the i-th μ-species particle ($\mu = \mathrm{L}, \mathrm{S}$). In Eqs. (S1) and (S2), the prime denotes that the summantion is taken over the particles for which $-0.3H \le y_i^{(\mu)} \le 0.3H$. Notice that the walls are located at $y = \pm 0.5H$. Additionally, $\hat{N}_\mu$ is the average number of μ-species particle in the region of $-0.3L \le y \le 0.3L$ and $\hat{\mathcal{A}}$ denotes the area of this region given by $\hat{\mathcal{A}} = 0.6\mathcal{A}$.

In the upper panels of Fig. S2, we show $g_{\mathrm{LL}}(\boldsymbol{r})$ at $\phi = 0.64$ for various values of $\dot{\gamma}$ in the shear-thinning regime, demonstrating that a structural anisotropy becomes evident with increasing $\dot{\gamma}$. Along the extension direction ($\hat{x} = \hat{y}$), the first peak of $g_{\mathrm{LL}}(\boldsymbol{r})$ becomes smaller and more broad towards the outer region with an increase in $\dot{\gamma}$, indicating that dilution occurs. On the other hand, along the

compression axis, almost the opposite occurs. Such behaviors are more clearly shown in the lower panels of Fig. S2, showing the cross-sectional views of $g_{\rm LL}(\boldsymbol{r})$ along the extension and compression axes. Note that essentially the same behaviors are observed for $g_{\rm SS}(\boldsymbol{r})$ and $g_{\rm SL}(\boldsymbol{r})$, which are not shown here.

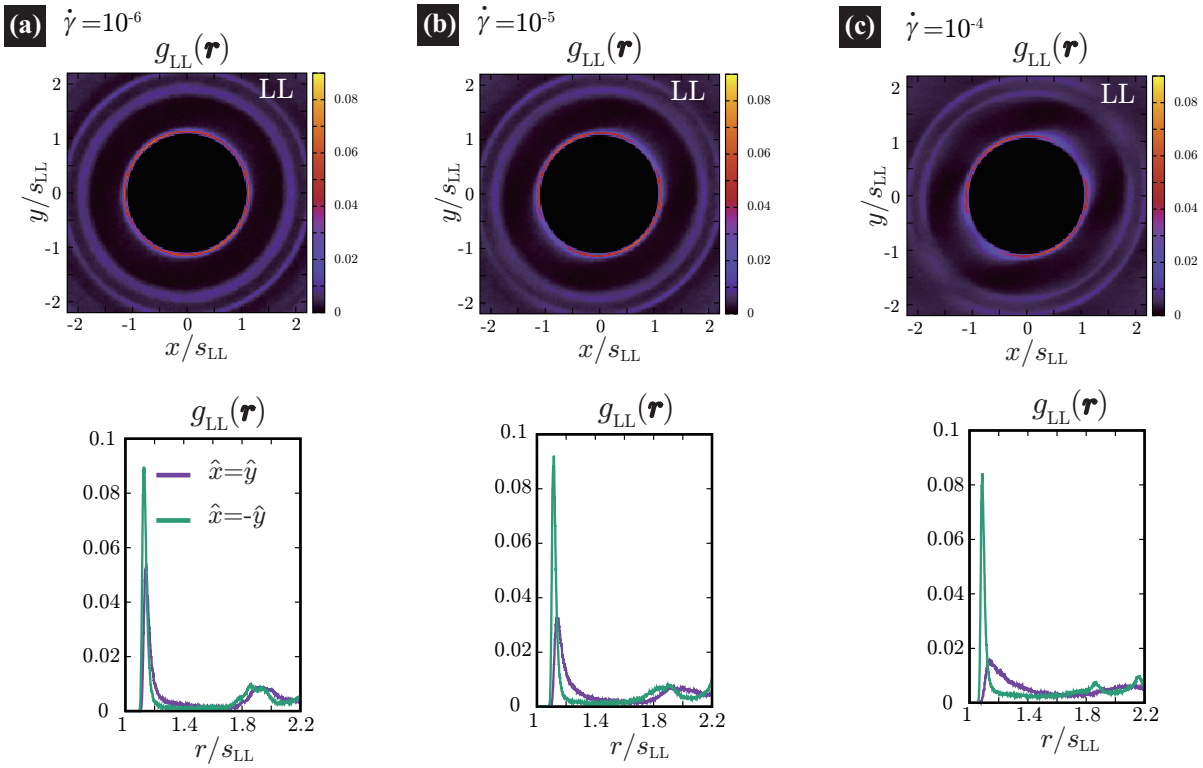

Fig. S2 $g_{\rm LL}(\boldsymbol{r})$ (upper) and its cross-sectional view (lower) for $\dot{\gamma} = 10^{-6}$ (a), 10^{-5} (b), and 10^{-4} (c). In the lower panels the purple and dark green lines represent $g_{\rm LL}(\boldsymbol{r})$ along the extension and compression axes, respectively.

These observations in the partial PDF are supplemented by measurements of the force bond. We represent the interaction force magnitude between the i- and j-th particles as $|f_{ij}| = |\partial U/\partial \boldsymbol{r}_{ij}|$ as the magnitude of the interaction forces between i- and j-th particles. In Figs. S3(a) and (d), we display typical snapshots of patterns of the force bonds, where the pairs of particles with non-zero interactions ($|f_{ij} > 0|$) are described by connecting bonds, for $\dot{\gamma} = 10^{-6}$ and 10^{-4}, respectively, at $\phi = 0.64$. Here, the color of each bond indicates the scaled value of $|f_{ij}|$ by $2\pi s_{\rm S} P_p$, with P_p being the particle pressure defined as[1]

$$P_p = -\frac{1}{2\mathcal{A}} \sum_i \sum_{j>i} \boldsymbol{r}_{ij} \cdot \frac{\partial U}{\partial \boldsymbol{r}_{ij}}. \tag{S3}$$

For the interaction potential used in this study, as given by Eq. (1), although the potential is steep, the cutoff distance is slightly longer than usual. Consequently, when we interpret particle pairs experiencing a non-zero interaction force as being in contact, most particles would be nearly in a perfect contact state for sufficiently large value of ϕ. Nevertheless, this interpretation is oversimplified. It is crucial to recognize that the characteristic force magnitude varies with the shear rate. As the shear rate increases, so does the driving external force, leading to a greater characteristic force. Therefore, if the interaction force between particles is significantly smaller than this characteristic force, these pairs can be considered ineffective in contact.

At this stage, identifying an exact threshold value for judging the interaction force as relevant for contact or not is still difficult. Instead, by adjusting the threshold value, bonds with force magnitudes below this threshold are not displayed, and subsequently, we assess how their overall patterns change with the shear rate. In Figs. S3 (b) and (c), at $\dot{\gamma} = 10^{-6}$, we display the same snapshots as (a) but with different threshold values. Furthermore, similar adjustments are made to (d), resulting in (e) and (f). A noticeable difference between the cases of $\dot{\gamma} = 10^{-6}$ and 10^{-4} is observed even for the threshold values of $|f_{ij}|/(2\pi s P_p) = 0.1$, It is observed that more bonds (mainly along the extension axis) disappear at higher shear rates: While larger forces are anisotropically exerted along the compression axis, forces along the extension axis are weaker, indicating an effective decrease in contact (or effective opening of gaps) along the elongation axis with an increase in the shear rate.

Before closing this section, it is noteworthy to mention the following point. Although we here scale the interaction forces by $2\pi s_{\rm S} P_p$, the characteristic force magnitude may be alternatively determined by particle shear stress. Notably, a similar trend was found when

the force is scaled by the shear stress.

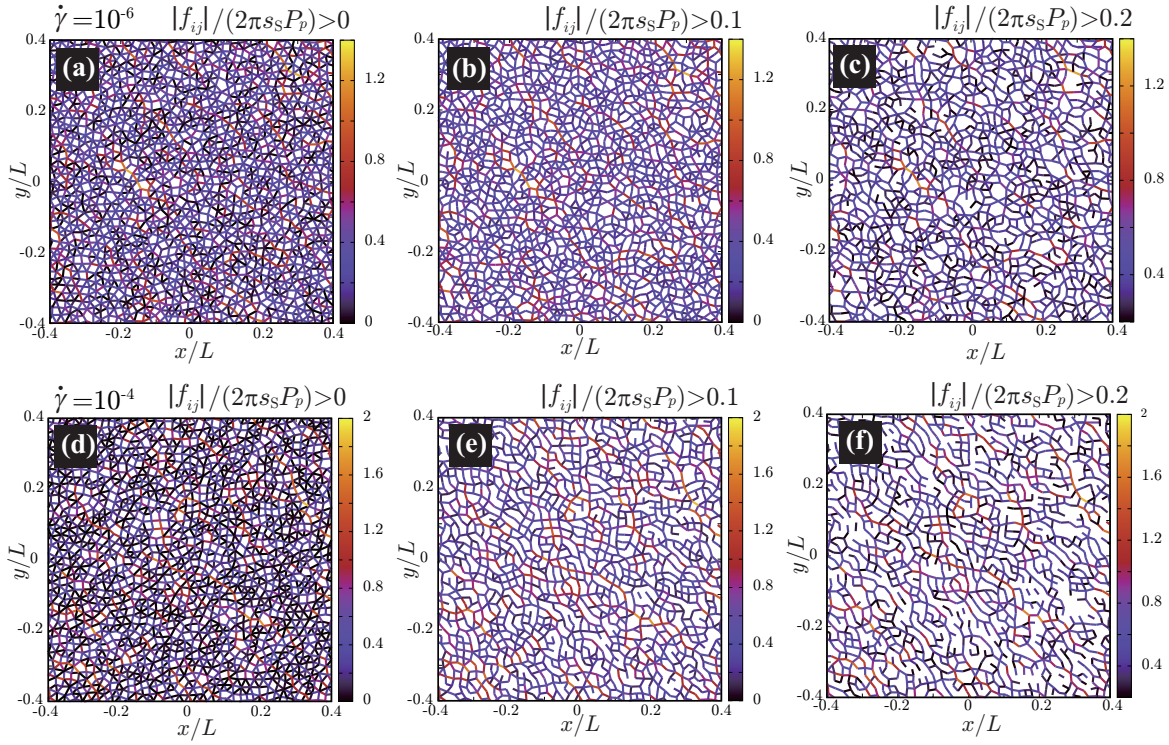

Fig. S3 Typical snapshots of the force-bonds at $\dot{\gamma} = 10^{-6}$ (a)-(c) and 10^{-4} (d)-(f) at $\phi = 0.64$ for various threshold values.

C Quantifying relative particle motion

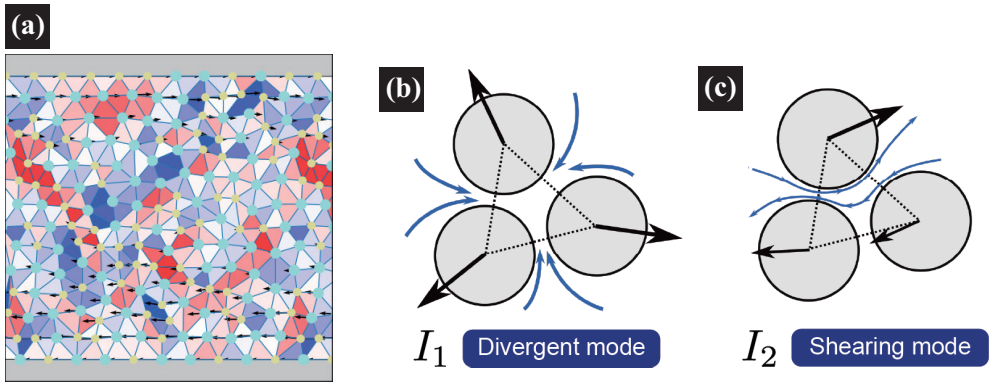

Fig. S4 (a) Snapshot of I_1. Each circle indicates the position of a particle, the color indicates the particle size, and the arrow indicates the velocity. Schematic pictures of I_1 (b) and I_2 (c). I_1 and I_2 measure the degree of divergent and shearing motions of the triangular element, respectively. The blue arrows schematically illustrate typical accompanying flows of the surrounding solvent.

We explain the details of our analysis of relative particle motion. To quantify the relative motion, we define two quantities, I_1 and I_2, whose physical meanings are schematically shown in Fig. S4: I_1 directly measures the rate of change of the triangular area, while I_2 measures the degree of shear deformation rate of the triangle. These quantities are calculated for each element. We perform Delaunay triangulation, in which the vertices are the positions of the particles $\boldsymbol{R}_i$. The solid lines in the left panel of Fig. S4 show the partitioning. The quantities I_1 and I_2 are tied to each triangular element. In this way, we can regard I_1 and I_2 as spatial variables.

Here, we define the two quantities I_1 and I_2 as invariants of a tensor. The derivation follows the simple procedure of the conventional finite element method (FEM)[2]. We pick up a triangular element e, whose vertices are numbered as $1, 2$, and 3 (see Fig. S5). We let f_i^e denote the value of an arbitrary variable $\tilde{f}$ at the vertex i ($i = 1, 2, 3$) on the element e. The vertex positions are denoted as (x_1^e, y_1^e),

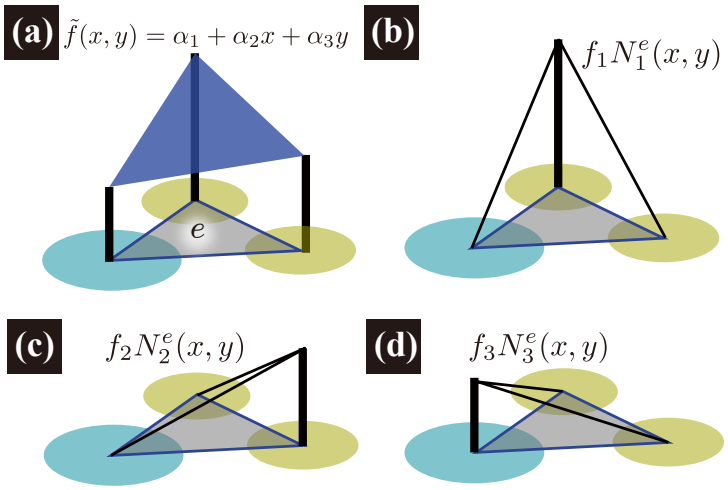

Fig. S5 (Left) A first-order triangular element. On each element, the approximate function $\tilde{f}(x,y)$ is described as a plane (a). The plane function $\tilde{f}(x,y)$ can be expressed as a product of shape functions $N_i^e(x,y)$ within the element and the values at the vertices f_i^e (b-d).

(x_2^e, y_2^e), and (x_3^e, y_3^e). Then, we formally express f_i^e as

$$\begin{pmatrix} f_1^e \\ f_2^e \\ f_3^e \end{pmatrix} = \begin{pmatrix} 1 & x_1^e & y_1^e \\ 1 & x_2^e & y_2^e \\ 1 & x_3^e & y_3^e \end{pmatrix} \begin{pmatrix} \alpha_1^e \\ \alpha_2^e \\ \alpha_3^e \end{pmatrix} =: S \begin{pmatrix} \alpha_1^e \\ \alpha_2^e \\ \alpha_3^e \end{pmatrix}, \tag{S4}$$

where the parameters $\begin{pmatrix} \alpha_1^e & \alpha_2^e & \alpha_3^e \end{pmatrix}$ are given by

$$\begin{pmatrix} \alpha_1^e \\ \alpha_2^e \\ \alpha_3^e \end{pmatrix} = S^{-1} \begin{pmatrix} f_1^e \\ f_2^e \\ f_3^e \end{pmatrix} \tag{S5}$$

with

$$\begin{aligned} S^{-1} &= \begin{pmatrix} a_1^e & a_2^e & a_3^e \\ b_1^e & b_2^e & b_3^e \\ c_1^e & c_2^e & c_3^e \end{pmatrix} \\ &:= \frac{1}{2A_e} \begin{pmatrix} x_2^e y_3^e - x_3^e y_2^e & x_3^e y_1^e - x_1^e y_3^e & x_1^e y_2^e - x_2^e y_1^e \\ y_2^e - y_3^e & y_3^e - y_1^e & y_1^e - y_2^e \\ x_3^e - x_2^e & x_1^e - x_3^e & x_3^e - x_2^e \end{pmatrix}, \end{aligned} \tag{S6}$$

where $A_e = \det(S)/2$. In the linear FEM, by defining the shape function as $N_i^e(x,y) = a_i^e + b_i^e x + c_i^e y \quad (i = 1,2,3)$, we express the field variable $\tilde{f}$ on the element e by interpolating the values assigned to the vertices as

$$\begin{aligned} \tilde{f}(x,y) &= \sum_{i=1,2,3} N_i^e(\boldsymbol{x}) f_i^e \\ &= \begin{pmatrix} N_1^e(x,y) & N_2^e(x,y) & N_3^e(x,y) \end{pmatrix} \begin{pmatrix} f_1^e \\ f_2^e \\ f_3^e \end{pmatrix}, \end{aligned} \tag{S7}$$

where $\boldsymbol{x} = (x,y) \in e$.

Let (V_{xi}^e, V_{yi}^e) be the velocity of the i-th particle on the element e. According to the above explained procedure, we can approximate

the particle velocity "field" at an arbitrary position $\boldsymbol{x}$ on the element e as the linear interpolation of (V^e_{xi}, V^e_{yi}):

$$V^e_x(\boldsymbol{x}) = \sum_{i=1,2,3} N^e_i(\boldsymbol{x}) V^e_{xi}, \tag{S8}$$

$$V^e_y(\boldsymbol{x}) = \sum_{i=1,2,3} N^e_i(\boldsymbol{x}) V^e_{yi}. \tag{S9}$$

Then, we can compute the deformation rate as

$$\begin{pmatrix} D^e_{xx} & D^e_{xy} \\ D^e_{yx} & D^e_{yy} \end{pmatrix} := \begin{pmatrix} \frac{\partial}{\partial x} V^e_x(\boldsymbol{x}) & \frac{\partial}{\partial x} V^e_y(\boldsymbol{x}) \\ \frac{\partial}{\partial y} V^e_x(\boldsymbol{x}) & \frac{\partial}{\partial y} V^e_y(\boldsymbol{x}) \end{pmatrix}, \tag{S10}$$

which further defines

$$I^e_1 := D^e_{xx} + D^e_{yy}, \tag{S11}$$

$$I^e_2 := (D^e_{xx} - D^e_{yy})^2 + (D^e_{xy} + D^e_{yx})^2. \tag{S12}$$

When a triangle is composed of particles of different sizes, even if the particle velocities exhibit isotropic symmetry, the associated flow of the surrounding solvent generally does not. However, in the current studies, I_1 and I_2 serve as measures to quantify the degree of volumetric and shear particle motions, respectively. It is not essential for the symmetry of particle motions to perfectly correspond with that of the solvent motions, although they are similar due to intrinsic dynamic coupling.

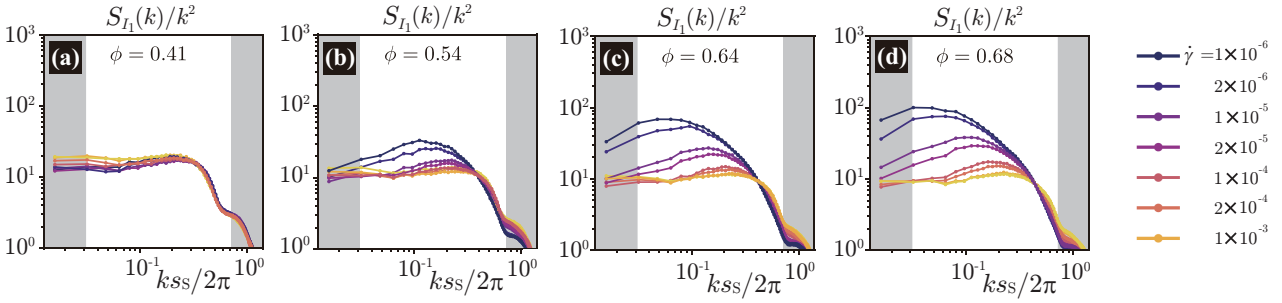

Fig. S6 $S_{I_1}(k)/k^2$ against $ks_S/2\pi$ at $\phi = 0.41$ (a), 0.54 (b), 0.64 (c), and 0.68 (d). At a lower k, enhancement of $S_{I_1}(k)$ is suppressed and behaves as k^a ($a \sim 2$).

To quantify the spatial correlation of the transverse and longitudinal particle motions, we define the following structure factors:

$$S_{I_1}(\boldsymbol{k}) = \frac{1}{\mathcal{A}} \langle |\hat{I}_1(\boldsymbol{k})|^2 \rangle, \tag{S13}$$

$$S_{I_2}(\boldsymbol{k}) = \frac{1}{\mathcal{A}} \langle |\hat{I}_2(\boldsymbol{k})|^2 \rangle, \tag{S14}$$

where $\hat{I}_m(\boldsymbol{k}) = \sum_e A_e \exp(-i\boldsymbol{k}\cdot\boldsymbol{R}^G_e) I^e_m$ (m=1,2) and $\boldsymbol{R}^G_e = (1/3)\sum_{i=1,2,3} \boldsymbol{R}_i$ is the geometrical center of the e-th triangular element. Note that, although a window function is not used here, the resultant structure factor for $k > 2 \times 2\pi/L$ is hardly altered by whether implementing it or not. In the continuum limit, it may be reduced to $\hat{I}_m(\boldsymbol{k}) = \int d\boldsymbol{r} \exp(-i\boldsymbol{k}\cdot\boldsymbol{r}) w(\boldsymbol{r}) I_m(\boldsymbol{r})$. As denoted in the main text, anisotropy and localization near the walls of the particle motions are not remarkable for the present ranges of ϕ and $\dot{\gamma}$, and thus we may safely replace $S_{I_m}(\boldsymbol{k})$ by its angle average $S_{I_m}(k)$.

Figures S6 and S7 display $S_{I_1}(k)$ and $S_{I_2}(k)$, respectively. As demonstrated in Fig. 5 in the main text, the regions with larger values of I_2 and i_2 almost correspond to each other, which indicates that stronger solvent dissipation is associated with larger relative shearing particle motion. This correspondence is further supported by Fig. S7: the spatial correlation of I_2 and its intensity grow as ϕ increases and $\dot{\gamma}$ decreases. Such tendencies of $S_{I_2}(k)$ are qualitatively similar to those of $S(k)$, the structure factor of i_2, which is shown in Fig. 4 in the main text. Unlike $S_{I_2}(k)$, Fig. S6 shows that an enhancement of $S_{I_1}(k)$ at the lower k is highly suppressed: as indicated in the main text, particle density increases and decreases occur alternatively in space at several particle length scales, which may suppress I_1 at larger scales. Since the rearrangement dynamics of particles are inevitably accompanied by solvent flows surrounding them, it is necessary to form flow channels by enhancing the particle gaps. However, the incompressibility of the solvent components tends to prevent particle density changes. The obtained form of $S_{I_1}(k)$ may reflect a compromise of these contradicting requirements. The impact of incompressibility on particle rearrangement dynamics will be discussed in more detail elsewhere[3].

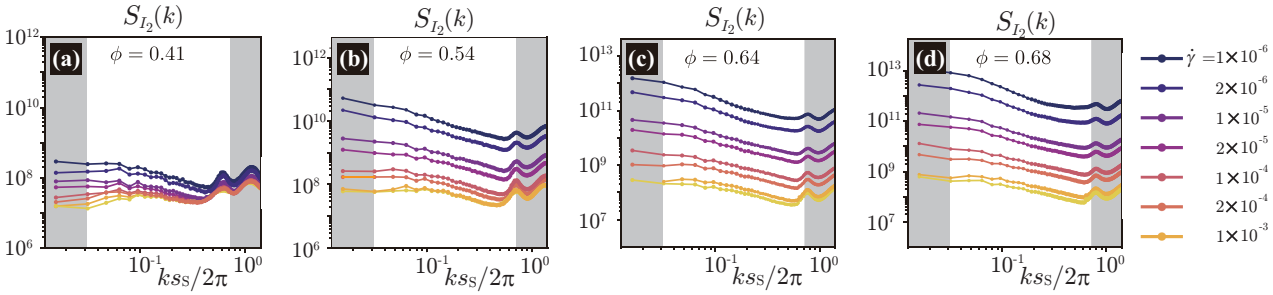

Fig. S7 Structure factor $S_{I_2}(k)$ of I_2 against $ks_S/2\pi$ at $\phi = 0.41$ (a), 0.54 (b), 0.64 (c), and 0.68 (d). For larger ϕ, $S_{I_2}(k)$ at lower k grows with decreasing $\dot{\gamma}$. Such behaviors are qualitatively similar to those of the structure factor of i_2 shown in Fig. 4 in the main text.

Notes and references

1 J-P. Hansen and I.R. McDonald, *Theory of Simple Liquids* (Academic Press, London and New York, 1976).

2 T. J. R. Hughes, *The finite element method: linear static and dynamic finite element analysis* (Courier Corporation, 2012).

3 T. Terayama and A. Furukawa, in preparation.